Probing lung function at high spatiotemporal resolution using a novel crystal ribcage

Rohin Banerji[1]†, Gabrielle N. Grifno[1]†, Linzheng Shi[1], Dylan Smolen[1], Rob LeBourdais[1], Johnathan Muhvich[1], Cate Eberman[1], Bradley Hiller[2], Jisu Lee[2], Kathryn Regan[1], Siyi Zheng[1], Sue S. Zhang[1], John Jiang[1], Riley Phil[2], Katrina Traber[2], Giovanni Ligresti[2], Joseph P. Mizgerd[2], Bela Suki[1], Hadi T. Nia[1*]

[1] Department of Biomedical Engineering, Boston University; Boston MA.
[2] Pulmonary Center, Boston University School of Medicine; Boston MA.
† Authors contributed equally to this publication
[*] Corresponding author. Email: htnia@bu.edu

Abstract:
Real-time, cellular resolution imaging is essential for probing the highly dynamic functions of the lung at the interface of physics, biology, and immunology. CT and MRI modalities have low spatial resolution, and histology provides only snapshots of fixed lungs with little temporal information. Existing intravital imaging approaches cannot image the spatiotemporal changes involved in respiratory function. Here, we present a novel, transparent "crystal" ribcage that provides a physiological environment for a functioning lung and allows high-resolution and real-time optical imaging of nearly the entire lung surface. This imaging capability is obtained while the crystal ribcage preserves the complex 3-D architecture, cellular diversity, and integrative function of the *ex vivo* ventilated and perfused lung at near *in vivo* conditions. Utilizing the crystal ribcage in health and lung diseases such as metastasis, pneumonia, and fibrosis, we (i) mapped how each disease differentially remodels the respiratory function of the lung at single alveolus level; (ii) determined the coupling between the circulation-respiration at the capillary level, and the compression of arrested cancer cells by capillaries during a breathing cycle; (iii) discovered that intravascular and interstitial, but not intra-alveolar neutrophils are reversibly responsive to vascular pressure; and (iv) found that metastatic nodules affect vascular transport functions up to 4-5 alveoli away from the tumor. Thus, combining the real-time visualization of the lung at high spatiotemporal resolution with precise modulation of respiration-circulation dynamics, the crystal ribcage opens the "black box" of the functioning lung and allows mechanistic probing of lung dynamic functions in health and disease.

The crystal ribcage enables dynamic cellular imaging of the lung in health and disease while controlling its physiology.

Introduction:
The lung is a mechanically active and highly dynamic organ, being exposed to cyclic deformations from a combination of respiration and pulsatile blood flow. The addition of the air-liquid interface makes it one of the most complex organs to probe in real-time at the subcellular level. Being continuously exposed to mechanical, biological, and immunological stresses, the lung is the site of many pathologies such as primary and metastatic cancers, pneumonia, fibrosis, and obstructive diseases. Understanding the complex and dynamic function of the lung in health and disease

requires characterization of structure and function at high spatial resolution to capture molecular and cellular dynamics, and at high temporal resolutions to resolve respiration-circulation dynamics such as vascular transport and cellular trafficking.

Current imaging modalities such as magnetic resonance imaging (MRI) and computed tomography (CT) lack the spatiotemporal resolution needed to resolve dynamic events such as alveolar deformation, capillary flow, and cellular activities. Histological analysis is commonly used to visualize a snapshot of the fixed lung tissue at subcellular resolution, however, dynamic biological and physical information relevant to respiration-circulation and cellular motility are lost. Recent intravital microscopy approaches are capable of imaging microcirculation dynamics in a limited region of the lung surface at high spatial resolution through a glass window placed over an opening in the ribcage [1-5]. Despite leading to key discoveries in lung immunology [5,6] and cancer metastasis [2,7], these methods do not allow normal respiratory function in the imaged region. In these approaches, the lung is immobilized against the glass using glue or suction thereby interfering with respiration at the region of interest [1-3,8]. The mechanical stretching-relaxing motion of the alveoli during breathing is tightly coupled to the biology and immunity of the lung in both health and disease [9-12]. To obtain a stable imaging surface these intravital microscopy methods exclude the effects associated to breathing motion in the imaging area. Furthermore, being limited to a small region of imaging, these approaches do not capture the lung heterogeneities (e.g., apex vs. base differences) and cannot track dynamic events outside the window of imaging (e.g., disease heterogeneities across the lung lobes).

Motivated by the recent progress in *ex vivo* whole-organ maintenance [13,14], we developed and validated Lung*E*x to visualize and mechanistically probe the real-time dynamics of a functioning lung at high optical resolution. The physics, biology and immunity of the *ex vivo* ventilated, perfused, and viable whole lung is preserved in Lung*E*x at near *in vivo* physiological conditions. Lung*E*x is equipped with crystal ribcage that provides physiological conditions for a functioning lung and allows high-resolution and real-time optical imaging. Utilizing the spatiotemporal resolution that this platform offers over nearly the entire surface of the lung, we, for the first time, mapped the spatial heterogeneities of alveolar deformations in healthy lungs, and quantified the alteration in alveolar deformation in multiple pulmonary pathologies such as cancer, pneumonia, and fibrosis. The large field of view provided by the crystal ribcage, combined with a novel computational platform, allowed us to probe the lung micro-physiology in response to respiratory and circulatory pressures at multiple scales, from the whole lung down to the alveolar, capillary, and single cell scale. Utilizing the unique capability of Lung*E*x in controlling the key respiratory and circulatory parameters, combined with the real-time imaging of cell migration, we showed that intravascular and interstitial, but not intra-alveolar neutrophils are strongly and reversibly responsive to hydrostatic vascular pressure. Finally, we demonstrated the capability of Lung*E*x in real-time imaging of drug delivery and retention in mouse models of acute lung injury, pneumonia, and breast cancer lung metastasis.

Results:

Development and validation of LungEx

Lung*E*x is composed of a ventilated and perfused *ex vivo* mouse lung housed in a transparent crystal ribcage (Fig. 1a-d, Supplementary Movie S1, Supplementary Movie S2). The crystal

ribcage is a biocompatible shell with a shape that recapitulates the native mouse ribcage to provide near-*in vivo* boundary conditions for the lung to slide against during ventilation and perfusion (Supplementary Movie S3). We designed the crystal ribcage based on µCT scans of the mouse lung [15-17] which was specific to the age and strain of interest (e.g., C57/BL6, AJ and FVB mouse strains in this study; fig. S1). For wider applications, we designed two versions of the crystal ribcage with unique capabilities: (i) a semi-flexible ribcage made from elastomer polydimethylsiloxane (PDMS) (Fig. 1e), and (ii) rigid ribcage made from polystyrene (Fig. 1f). Both PDMS and polystyrene are widely used for biological applications as they are biocompatible and lack any autofluorescence. Our rationale for the development of the flexible crystal ribcage was to account for the deformation of the ribcage that contributes to lung ventilation, particularly during deep inspiration. However, since the PDMS crystal ribcage cannot function in negative-pressure ventilation, the mode that closely recapitulates spontaneous breathing, we designed the rigid ribcage to allow both positive- and negative-pressure ventilation. Since normal quiet breathing is accomplished almost entirely by the movement of the diaphragm [18] (fig. S2), the rigid crystal ribcage was used in most of the studies presented here. For both versions of crystal ribcage, we started from µCT scans of the native mouse ribcage (Fig. 1c) and used multiple steps of additive, sacrificial, and thermo-forming fabrication processes (Fig. 1e and f) to reach a nearly uniform thickness of 150 µm (similar in thickness to No. 1.5 glass coverslip: fig. S3a). With this thickness, we were able to use both air and water immersion objective lenses with a wide range of working distances. Next, we engineered the internal surface of the crystal ribcage to be durably hydrophilic (Fig. 1h) similar to the intact ribcage in the mouse, which substantially reduced the friction between the lung and the crystal ribcage (see Methods).

We validated the image quality and functionality of the crystal ribcage in multiple ways: first, we ensured that hydrophilicity of the internal surface of the crystal ribcage is maintained, at different anatomical locations, for at least 6 hours (Fig. 1h). Unlike the current intravital microscopy approaches that work with a flat glass slide, our crystal ribcage conforms to the lung's curvature to preserve the lung geometry and motion. Second, we imaged fully spherical beads as a test sample to validate that the curvature of the crystal ribcage does not cause optical aberrations (fig. S3b). Finally, we showed that the alveolar deformations in the crystal ribcage are comparable to the intact mouse ribcage throughout the breathing cycle (Fig. 1i). To do so, in an intact ribcage from a freshly sacrificed mouse, we locally removed the muscles in between ribs to make a small opening while preserving the pleural membrane, to image the underlying alveoli *in situ* by optical coherence tomography (OCT) which allows for deep label-free imaging. We then excised the lung and positioned it in the crystal ribcage to image over the same region *ex vivo*. Comparing the breathing dynamics and the alveolar diameters in situ vs in the crystal ribcage, we demonstrated that the crystal ribcage closely mimics the actual breathing motions of the mouse ribcage.

Unlike most biological imaging applications that rely on imaging through a flat surface, our curved crystal ribcage required a new setup to be mounted on commercial optical microscopes. Therefore, we developed a 6 degree of freedom arm-fixture (fig. S4) that allowed orientation of the crystal ribcage to any desired angle and position with respect to the objective, and hence provided a nearly full-surface imaging capability of the lung. We further designed a compact module that housed the required sensors (flow and pressure) for both the ventilation and circulation systems next to the crystal ribcage to minimize dead space (Fig 1b). Finally, our system was equipped with a commercial and custom-made ventilator and a perfusion pump for precise control over lung

physiology in different settings such as negative- vs. positive-pressure ventilation and steady vs. pulsatile vascular flow. The whole platform, mounted on a cart, was designed to be portable to move between different microscopes (fig S4).

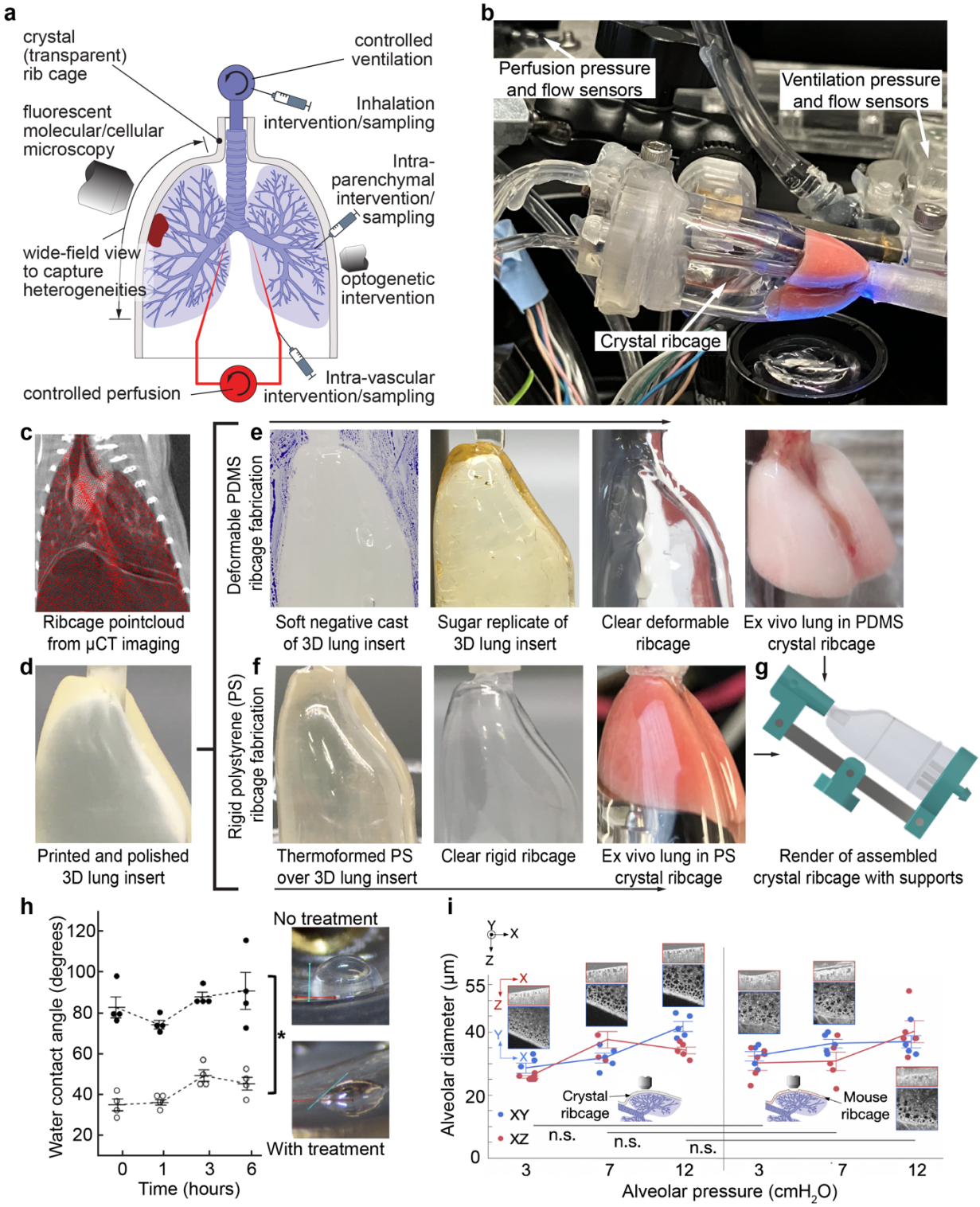

Fig. 1. Development and validation of a novel crystal ribcage and its integration into the Lung*E*x platform. (**a**) Schematic representation of the age- and strain-specific crystal ribcage and Lung*E*x to image over the entire *ex vivo* lung surface using a wide range of optical microscopes, with controlled ventilation and circulation parameters. (**b**) A functional mouse lung in the crystal ribcage supported by Lung*E*x with the control-sensing block positioned immediately next to the crystal ribcage. (**c**) A native mouse ribcage point cloud generated by processing µCT data,

converted into a 3D printable object. (**d**) Final polished 3D-insert of the model mouse ribcage, used for both semi-deformable PDMS ribcage fabrication (**e**) and rigid polystyrene crystal ribcage fabrication (**f**). Crystal ribcage is assembled with necessary supports (**g**) to integrate with a 6 degree of freedom mounting arm. (**h**) The engineered crystal ribcage surface maintained durable hydrophilicity, measured via water contact angle; data presented as mean ± S.E.M. for n=4 water droplets in different regions of the ribcage. (**i**) Alveolar deformation in crystal ribcage vs. an intact mouse ribcage shows no significant difference in diameter for n = 5 alveoli in each sagittal (XZ) and axial (XY) view, data reported as mean ± S.E.M. validating the physiological function of the lung in the crystal ribcage.

Mapping alveolar deformation heterogeneities in health and disease

We utilized Lung*E*x to probe alveolar deformation and heterogeneities in health and key pulmonary diseases including pneumonia, fibrosis, and lung metastases with different growth patterns. We, for the first time, imaged the functional mouse lung at multiple scales starting at the whole lung level (Fig. 2a, f, k, p, u) and the lobe level (Fig. 2b, g, l, q, v), and down to the alveolar level (Fig. 2c, h, m, r, w). At all these scales, the images were acquired over a physiological range of alveolar pressures of 3, 7, 12, and 18 cmH_2O. The unique capability of Lung*E*x in tracking and imaging the same region of interest at different alveolar pressures allowed us to assess key mechanical characteristics of the lung such as sub-alveolar resolution strain maps and single-alveolus pressure-volume curves. While the stiffness heterogeneity of the lung has previously been investigated using atomic force microscopy (AFM) in sectioned frozen tissue [19], our system enables the generation of strain maps (Fig. 2d,i,n,s,x) in a functional and intact lung where the 3D architecture and air-liquid interface are preserved. Notably, the multiscale capability of Lung*E*x allows us to probe wide fields of view (e.g., apex to base fig. S6, Supplementary Movie S4, Supplementary Movie S5), to better capture the heterogeneities in the physical functions of the lung. Similarly, the pressure-volume response, a classical functional index that is sensitive to lung stiffening as observed in fibrosis, pneumonia, and cancer) or softening (as in emphysema), has previously been reported only at the whole-organ level. Using our *ex vivo* system, we characterized the pressure-diameter responses of the lung at single-alveolus resolution. Here, we report alveolar diameters (Fig. 2u-y) instead of volumes for a more intuitive representation (pressure-volume curves shown in fig. S7). Quantifying the response of individual alveoli to pressure changes (each datapoint in Fig. 2e, j, o, t, y represents a single alveolus), enables us to better understand the natural heterogeneity of lung micromechanics. We first observed that while the average alveolar diameter changed from 28 µm at 3 cmH_2O to 42 µm at 18 cmH_2O, the alveolar diameters displayed a wide range of distribution at each pressure level. Unexpectedly, the heterogeneity in alveolar diameters increased when pressure was increased (Fig. 2y).

The lung is one of the major sites of metastasis for many cancer types including breast cancer [20]. Hence, we probed how the alveoli are remodeled by early-stage metastatic tumors, which was previously probed only in large tumors and via invasive approaches [21,22]. We were particularly interested in probing the effects of growth pattern on remodeling of the septal walls. According to our work [23] and others' [24], tumor growth patterns have been categorized as *nodular* (growth as a dense ball that pushes the existing normal tissue away) as opposed to an *infiltrative* growth pattern (replacing the existing normal cells with minimal remodeling effects on their surrounding), with distinct biological and clinical outcomes. Here, we demonstrate that both nodular and infiltrative growth patterns occur in early stages of breast cancer lung metastasis in mice. We used the fluorescently labeled murine breast cancer cell lines MMTV-H2B-dendra2 and E0771-H2B-dendra2, which presented nodular and infiltrative growth patterns, respectively. We observed

much denser tumors in the case of the MMTV tumors reflected in the organ (Fig. 2f), lobe (Fig. 2g), and alveolus levels (Fig. 2h). Interestingly, in nodular growth pattern (Fig. 2i), we observed much smaller strain values (i.e., very stiff) intratumorally compared to the infiltrative tumor with similar diameters (Fig. 2n). Intriguingly, due to the "pushing" effect of the nodular tumor, alveoli remained distended even at low alveolar pressures (Fig. 2j), while the alveoli in the infiltrative tumors change diameters with pressure similar to those far from the tumor (Fig. 2o). This single-alveolar scale observation of differential lung remodeling by different types of tumor growth will inform future studies on the effects of growth pattern on tumor progression, tissue remodeling, immune evasion, and treatment response.

Next, we probed the remodeling of single alveoli by pneumonia. We used a left lobar model of bacterial pneumonia (*Streptococcus pneumoniae* serotype 3, Sp3) induced in MRP8-mTmG reporter mice, where the MRP8+ cells (neutrophil dominant [25]) express green fluorescent protein (GFP) in the cell membrane. The whole-lung level imaging through the crystal ribcage shows the hepatized left apex (Fig. 2p), densely packed with MRP8+ neutrophils at both the lobe (Fig. 2q) and alveolar scales (Fig. 2r). Surprisingly, the alveoli that were affected by pneumonia showed equal or even greater stiffening compared to nodular tumors (Fig. 2s,i). We also observed more heterogeneities in alveolar diameter, not only in the infected areas, but in the alveoli adjacent to them (Fig. 2t). While we probed mainly the MRP8+ regions, we observed vast heterogeneities (fig. S8) in the infected areas without any MRP8+ cells that showed no response to change of alveolar pressure (likely due to edema). Finally, we probed pulmonary fibrosis as another key lung disease. We applied the bleomycin model of lung fibrosis on Col1a2-Cre-mTmG reporter mice [26]. Lung cells of this transgenic mouse are labeled tdTomato and those with an active Col1a2 promoter become GFP-labeled upon tamoxifen administration (see Methods). By taking advantage of the whole lung fluorescence, we identified dense fibrotic patches in the alveolar structure imaged using tdTomato and fibroblast aggregates using GFP (col1a1-mTmG; fig. S9). We observed that while alveolar deformation and strain have increased because of the disease progression, these alterations were not as drastic as those observed in pneumonia (Fig. 2s,x).

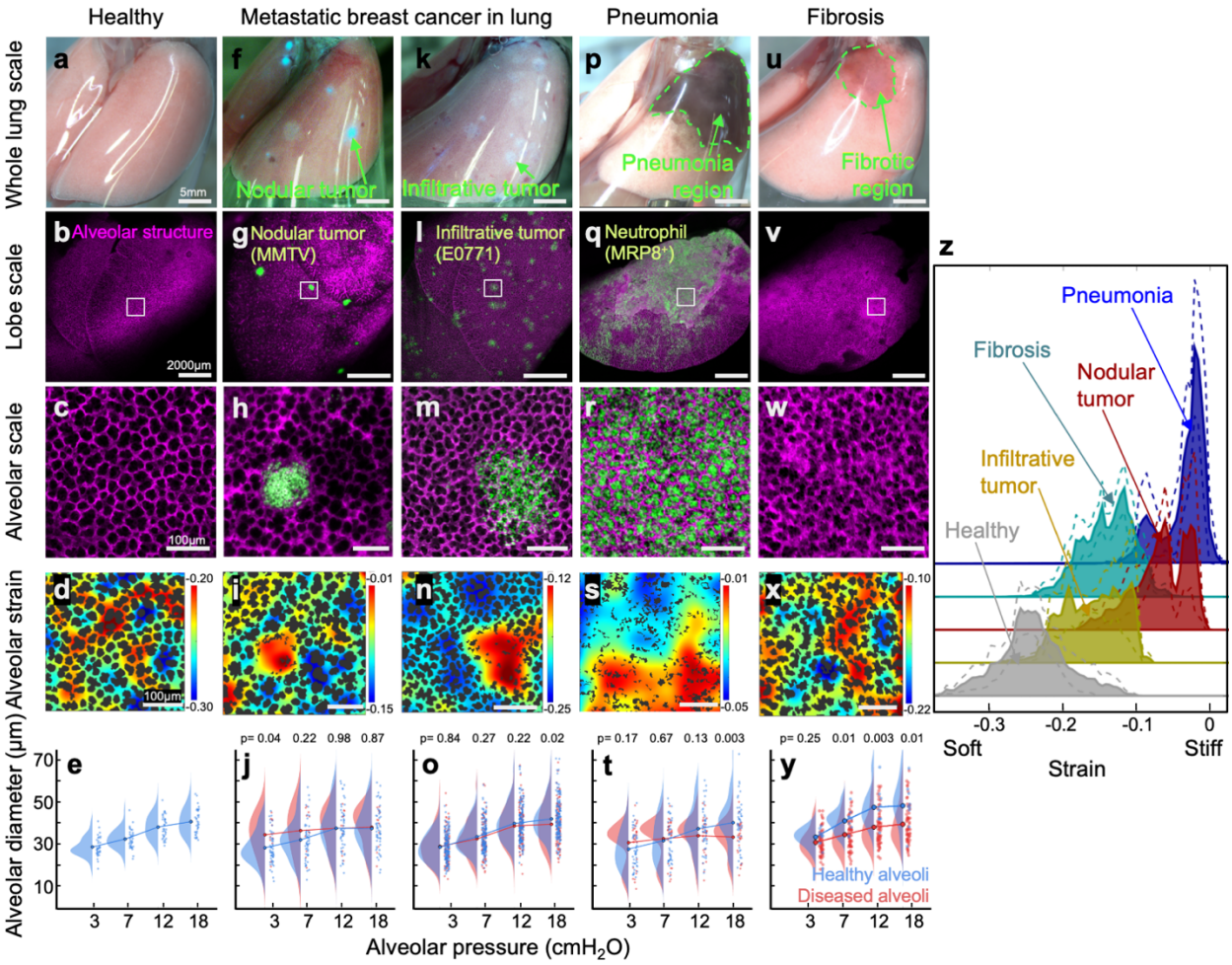

Fig. 2. The crystal ribcage allows multi-scale analysis of lung micromechanics in health and disease. Representative multiscale images of the lung visualized through the crystal ribcage in health (alveolar structure in magenta by using mTmG) (**a-c**), nodular metastasis (MMTV; tagged with dendra fluorophore in green) (**f-h**), infiltrative metastasis (E0771; tagged with dendra fluorophore in green) (**k-m**), pneumonia (Sp3; MRP8+ neutrophils in green) (**p-r**), and fibrosis (bleomycin injury) (**u-w**). The functioning lung has been visualized at the whole-lung (**a, f, k, p, u**), lobe (**b, g, l, q, v**), and alveolar (**c, h, m, r, w**) scales. The alveolar scale view of the lung in health and disease was used to map the strain (related to stiffness) at the sub-alveolar view (**d, i, n, s, x**), and generated single-alveolus pressure-diameter curves (**e, j, o, t, y**). All alveolar scale images were recorded at a pressure of 7cmH_2O, and the strain map was obtained by comparing the alveoli at 7 and 12 cmH_2O. For all disease conditions, the average strain distribution results (**z**) are based on n = 4 mice, except pneumonia that included n = 3 mice. We used k > 30 alveoli per mouse per disease condition with n = 3 mice per condition, except infiltrative tumor condition that had n = 4 mice.

Respiration-circulation coupling at the capillary and single cell levels

We took advantage of the unique capability of Lung*E*x to modulate lung circulation and ventilation independently while imaging of the vascular distensibility (change in diameter) at the capillary level and arteriole/venule levels to probe circulation-ventilation coupling. These assessments have been limited to large blood vessels in the field [27] and cannot be fully achieved in existing *ex vivo* and *in vivo* models. We increased the quasi-static alveolar air pressure from 3 to 18 cmH_2O, and hydrostatic vascular pressures from 0 to 15 cmH_2O to capture the change of diameters in blood vessels in response to physiological range of pressure values [27] (Fig. 3a; fig. S10). We observed that the arteriole/venule diameters reached a maximum at intermediate air pressures, between 7

and 12 cmH_2O (Fig. 3b), while the capillary diameter reached its maximum at a lower pressure of 7 cmH_2O (Fig. 3c). This interesting pressure response implies that there is an optimum alveolar pressure that maximizes the capillary and arteriole/venule diameters also minimizing the vascular resistance. To our knowledge this is the first observation of tight respiration-circulation coupling at the capillary level in a functional lung.

Next, explored how changes in vascular diameter affect the circulating cells, such as cancer cells, which have diameters equal or larger than those of the capillaries. We perfused labeled breast cancer cells (E0771-H2B-dendra2; green nucleus; far red membrane) into the lungs via intracardiac injection and imaged the arrested cells through the crystal ribcage (Fig. 3d-f). From the full-lobe view of the lung, we first identified single clusters of arrested cells of interest and easily navigate to those regions to image single cell deformations with changing alveolar pressure. We measured the deformation of cells arrested in capillaries (Fig. 3e) and arterioles/venules (Fig. 3f) in response to decreasing alveolar pressure from 18 to 3 cmH_2O. We quantified cellular deformation using the Feret ratio (the ratio of maximum to minimum caliper width of the cell; Fig. 3g). Interestingly, we observed that as alveolar pressure increased, single cells in capillaries had an increasing trend in Feret ratio while cells arrested in larger arterioles/venules were almost unchanged. We also observed that the difference in the Feret ratio for cells in capillaries vs larger arterioles/venules was statistically significant for an alveolar pressure of 3 cmH_2O, indicating that cancer cells undergo a dramatic deformation, and hence, experience substantial mechanical forces, when arrested in capillaries. These findings will have implications in determining how contact forces from capillaries, that change in response to alveolar pressure, affect sequestration and extravasation of immune and cancer cells into the lung interstitium [1,2].

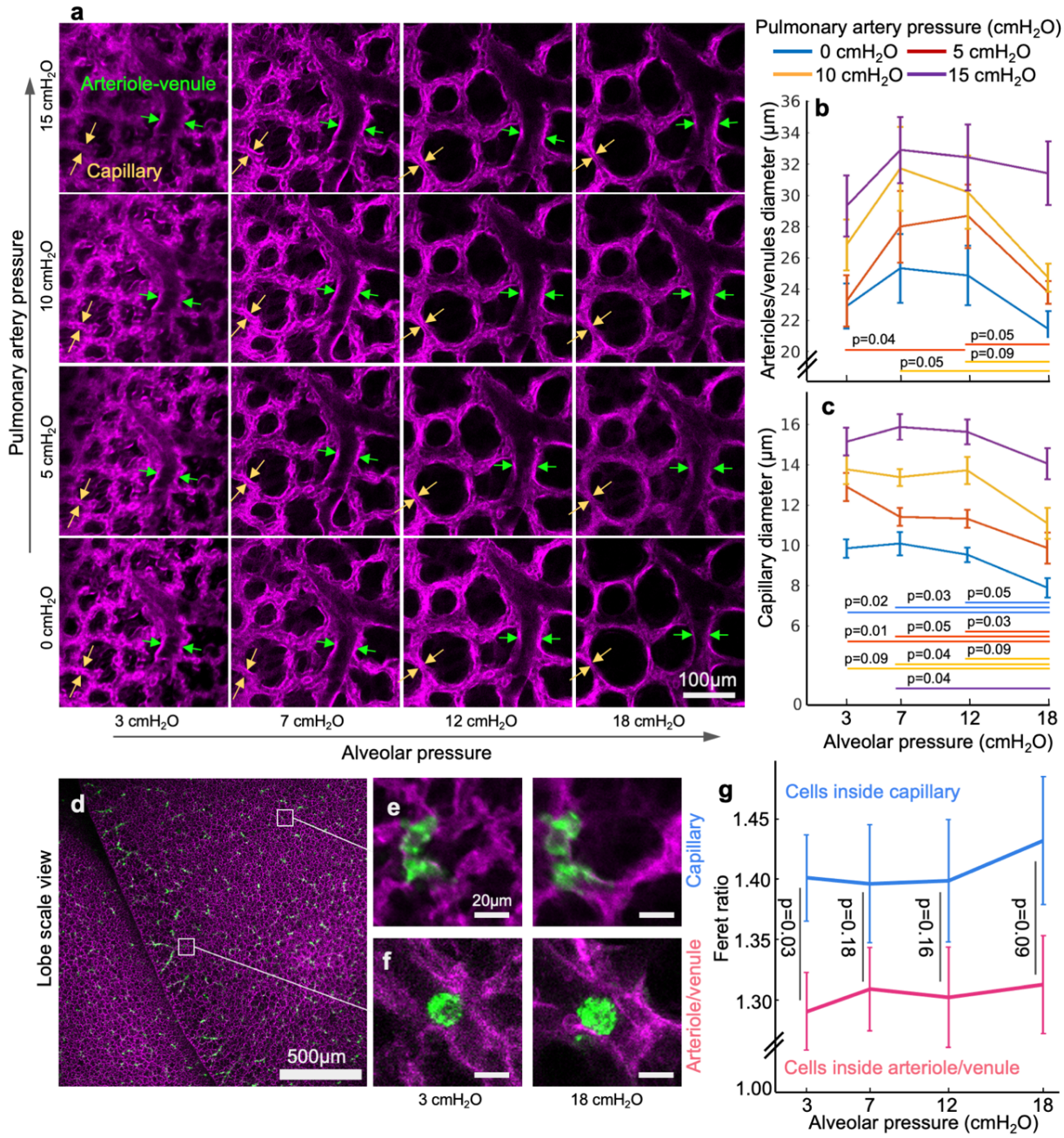

Fig. 3. Vascular distensibility and single cell deformation in response to alveolar and vascular pressure. (**a**) Representative image of both the arteriole/venule indicated by green arrows and capillaries in yellow arrows to show changing distensibility with increasing alveolar pressure and vascular pressure. Quantified arteriole/venule (**b**) and capillary diameter (**c**) with changing alveolar pressure. Single E0771-H2B-dendra2 cancer cell (green) distribution in lungs imaged at the mid-lobe scale (**d**) and subsequently cellular scale to show deforming cell shape in capillaries (**e**) and arterioles/venules (**f**) in response to alveolar pressures of 3 and 18 cmH_2O. The deformation is reported as the Feret ratio (**g**) which is tracked for the same cells across n = 30 cells in arterioles/venules group and n = 40 cells in capillaries pooled from n = 6 mice. The Feret ratio is significantly larger for cells in capillaries than in arterioles-venules when the lung is most relaxed at 3 cmH_2O. Data in **b, c, g** presented as mean ± S.E.M.

Active neutrophil migration is highly responsive to hydrostatic pressure

Neutrophils traffic into the lung in response to injury and infection [28]. While intravital microscopy has visualized immune trafficking in the lung [29], probing neutrophil migration dynamics under normal respiratory and circulatory conditions remain challenging *in vivo*. Using the Lung*E*x, we were able to overcome this challenge and assess neutrophil migration within the lung in real-time under controlled, (patho)physiologically relevant alveolar and vascular pressures. We recruited neutrophils (green fluorescent MRP8+) to the lung by intratracheally injecting either bacterial lipopolysaccharides (LPS) [30,31] or Sp3 bacteria [32] into the left lobe of the lung, to model acute injury and lobar pneumonia, respectively. Three hours post LPS injection, imaging through the crystal ribcage revealed that neutrophils were recruited to the lung and were most abundant at the left apex (Fig. 4a). Neutrophils recruitment was even greater in injured sites in the pneumonia model (imaged 24-36 hours post injection) (fig. S8).

While neutrophil responsiveness to shear stresses and cyclic pressure has previously been reported [31,33-35], we show that migration of neutrophils in the lung is highly dependent on hydrostatic vascular pressure (Supplementary Movie S6), in the absence of perfusate flow and shear stresses. By real-time tracking of neutrophils at vascular pressure of 0 and 15 cmH_2O under no flow conditions and a constant alveolar pressure of 7 cmH_2O, we found that neutrophils were substantially more migratory and traveled a longer distance over 5 minutes at higher perfusate pressures (Fig. 4b, fig. S11). Simultaneously, we observed no significant change in the persistence of neutrophil migration (defined as ratio of final cell displacement to the total length of the migration path) (Fig. 4d), with the varying vascular pressure. Interestingly, this dramatic increase in neutrophil velocity by elevation of hydrostatic pressure was fully reversible, and the neutrophils slowed down once the hydrostatic pressure was lowered (Fig. 4c, fig. S12). However, in the pneumonia model, we observed a similar increase in speed for increasing hydrostatic pressure, and further delineated the mechanosensitivity of different populations of neutrophils (Fig. 4e, f). Intravascular and interstitial neutrophils were both highly sensitive to pressure increases, while intra-alveolar neutrophils that were packed tightly in the air spaces were less motile and persistent (a measure of directionality), and their migration was independent of vascular pressure (Fig. 4g, h).

Additionally, we also found that neutrophils are physically deformed while migrating inside the vascular lumen and alveolar septa near the sites of pneumonia injury (Fig. 4i, Supplementary Movie S7), and cell deformation directly correlated with migration speed. We applied a constant alveolar pressure of 7 cmH_2O and vascular hydrostatic pressure of 7 cmH_2O under zero flow conditions and longitudinally tracked neutrophils at single cell resolution and observed that their instantaneous speed increased with increasing aspect ratio and decreasing circularity (Fig. 4j). Taking a linear regression of the instantaneous speed plotted against both parameters showed a positive correlation with aspect ratio and negative correlation with circularity for a population of neutrophils. (Fig. 4k).

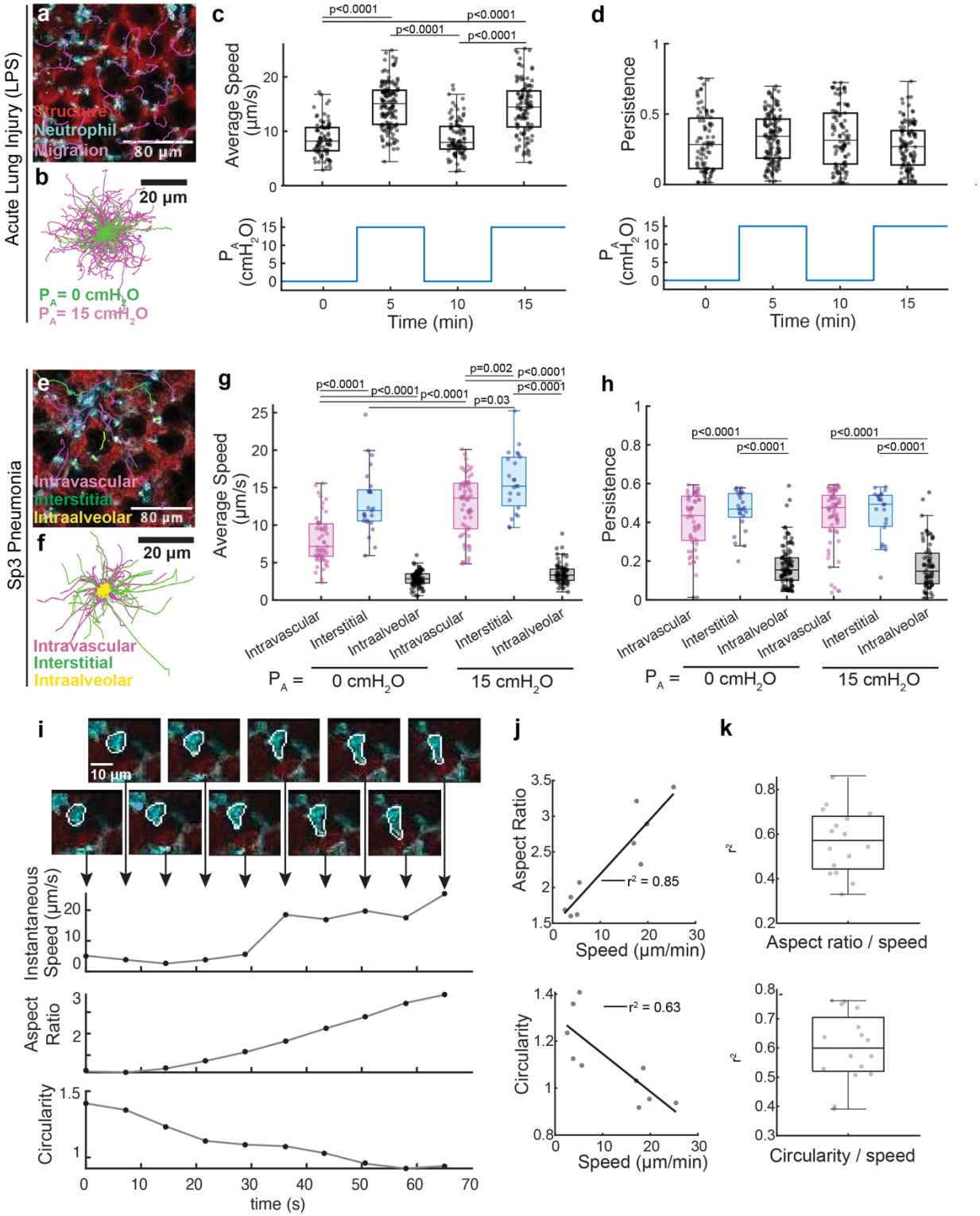

Fig. 4. Mechanosensitivity of neutrophils to hydrostatic pressure. (**a**) Representative image of neutrophil migration with cell trajectories (magenta) in the LPS model of acute lung injury. (**b**) Neutrophil migration map over a 5-minute imaging interval, (**c**) Neutrophil average speed increases with vascular pressure and is reversible in LPS-damaged lungs (n = 3 mice). (**d**) Persistence directionality of neutrophil migration in LPS-damaged lungs. I Representative traced neutrophil migration in intra-alveolar (yellow), interstitial (cyan), and intravascular (magenta) spaces in Sp3

pneumonia lungs at a pulmonary artery pressure (P_A) of 15 cmH_2O. (**f**) Neutrophil migration map for 15 cmH_2O hydrostatic perfusion pressures in pneumonia lungs for 5 minutes. (**g**) Neutrophil average speed and **(h)** persistence directionality in intra-alveolar, interstitial, and intravascular spaces under 0 or 15 cmH_2O hydrostatic perfusion pressures in pneumonia lungs (n = 3 mice). **(i)** Representative changes in single neutrophil speed, aspect ratio, circularity of the same neutrophil with its **(j)** respective aspect ratio vs. speed and circularity vs. speed regressions. **(k)** The regression coefficient of determination of aspect ratio vs. speed and circularity vs. speed of a population of neutrophils (n = 27 cells pooled across n = 3 mice). Box charts indicate median, upper and lower quartiles, and maximum and minimum values that are not outliers of the scattered datapoints.

Vascular transport dynamics are altered in lung cancer and pneumonia

We utilized Lung*E*x to study the spatial and temporal distribution of small molecular weight fluorescent tracers in the lung vasculature, with the aim of modeling the spatiotemporal delivery of small molecular weight drugs. We probed the vascular delivery of tracers in healthy, metastasis, and pneumonia models in mice. We used Cascade Blue fluorescent dextran (CBdextran, 10 kDa), and cascade Blue Hydrazide Trilithium salt (CBhydrazide, 500 Da) to model water-soluble, small molecular weight drugs. First, using the crystal ribcage, we imaged the transport dynamics of a 50 µL bolus of dye to model an impulse delivery (Fig. 5a, Supplementary Movie S8) under 15 cmH_2O of pressure-controlled flow of approximately 2 ml/min across the surface of the healthy lung, approximating the median pressure at the mouse pulmonary artery [36]. From the timelapse images (Fig. 5b), we quantified the maximum and duration of fluorescence intensity across the capillary bed and determined the heterogeneities of vascular transport in the healthy alveoli (Fig. 5e). The maximum color intensity was observed in the larger arterioles/venules while capillaries showed reduced intensity, indicating that capillaries may not be as perfused as the larger arterioles/venules.

We then used the nodular growth tumor model of breast cancer lung metastasis using the MMTV-dendra2 cancer cells, under the same conditions as the healthy lung. Time lapse imaging of the dye transport in the peri-tumor region revealed that the dye is excluded from the peritumor and intratumor areas, indicating that the native blood vessels near the tumor are not functional (fig. S13, Supplementary Movie S8) and further allowing us to quantify mean peritumor thickness as ~100 µm (fig. S14). However, far from the tumor, the capillary bed remained functional, and vascular transport dynamics were similar to what we observed in healthy lungs (Fig. 5c, e,f).

Next, we investigated transport dynamics in bacterial pneumonia. CBhydrazide dye transport (50 µL bolus of 10 mg/ml solution) in the pneumonia region (Fig. 5d) revealed that vascular transport is spatially heterogeneous near the pneumonia injury with respect to the distribution of the fluorescence intensity (Fig. 5e,f, Supplementary Movie 8) and time duration of fluorescence intensity (Fig. 5g). Quantification of transport dynamics revealed that overall fluorescence intensity in the pneumonia-injured region trended towards being higher than less-injured areas across all observed timepoints (Fig. 5f). However, in comparison to the peritumor region the time course of vascular transport was less affected in pneumonia injured regions in that the time to maximum intensity during the bolus transport (fig. S14), normalized fluorescence signal intensity (Fig. 5f) and T_{50}, the duration that the dye is greater than 50% of the maximum normalized intensity (Fig. 5g), was similar in pneumonia injury and the healthy-looking surroundings.

Lastly, we demonstrated that the Lung*E*x system was uniquely able to study direct diffusion of small molecular weight tracers in case of nodular growth metastatic tumors independent of flow-mediated (vascular convection) transport. We perfused CBhydrazide dye into the lung at a concentration of 0.25 mg/ml until the average fluorescence in the vessel lumens appeared to reach

a steady state (Fig. 5h). Next, we maintained the lung at a constant perfusate pressure of 5 cmH_2O at the pulmonary artery, without bulk flow traveling through the vessels, and a constant alveolar air pressure of 7 cmH_2O. Having eliminated convection-driven transport through the vessels, we imaged diffusion of the small molecular weight CBhydrazide dye into the tumor nodule in response to the applied step-increase in transport tracer over 1 hour (Fig. 5h). At t = 0 minutes, the blood vessel lumens surrounding the nodule were filled with dye; however, majority of the tumor bulk still excluded the dye. (Fig. 5i). After 60 minutes, the dye has diffused noticeably into the tumor bulk, but the dye surrounding blood vessels appears mostly unchanged. We quantified the increase in fluorescence intensity inside the tumor normalized by the background intensity over time. While the background intensity remained largely constant, the fluorescence intensity (directly correlated with tracer concentration) in the tumor ROI increased steadily over one hour (Fig. 5j).

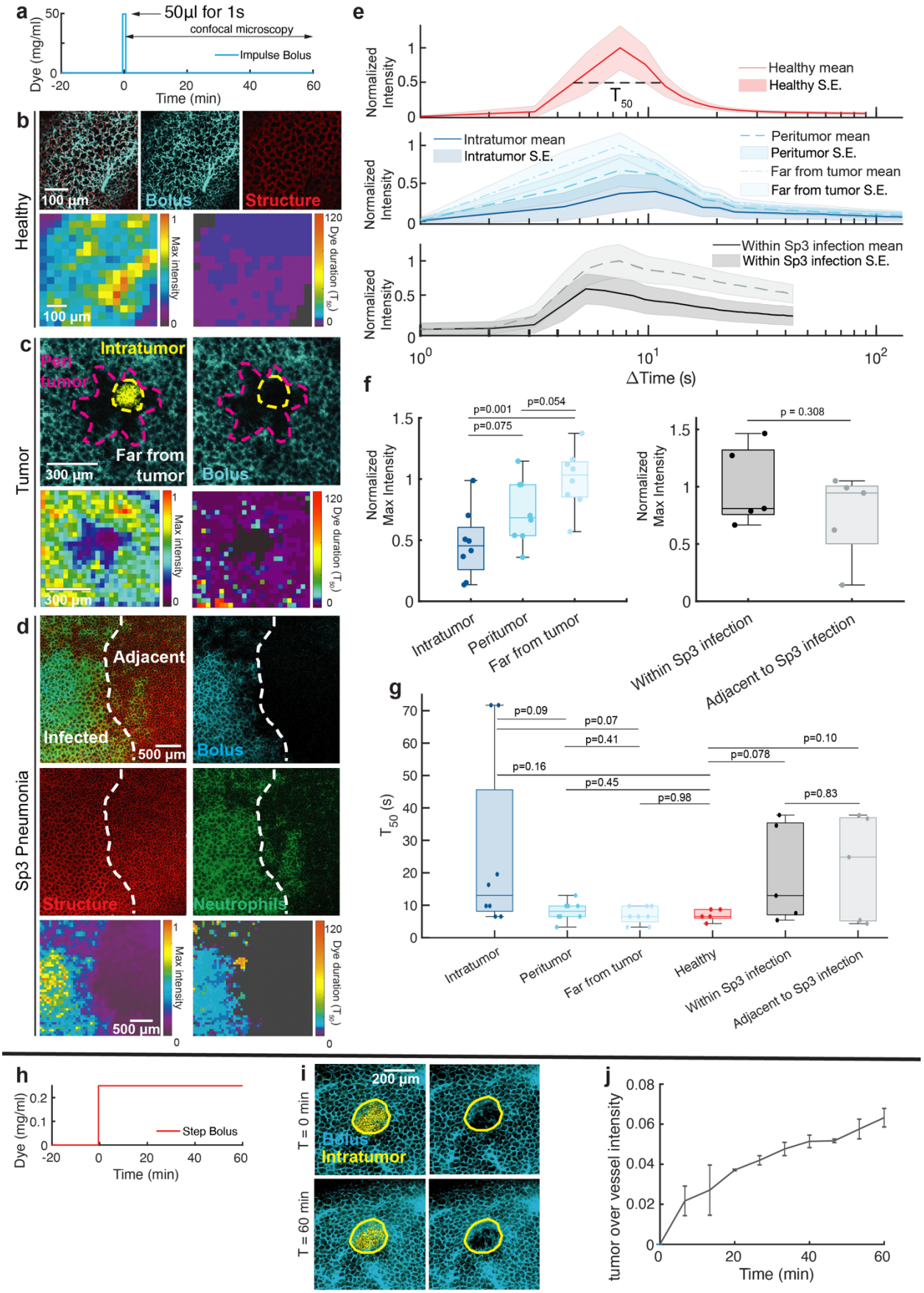
a
50µl for 1s
confocal microscopy
Impulse Bolus
Dye (mg/ml)
Time (min)
b
Healthy
100 µm
Bolus
Structure
Max intensity
Dye duration (T_{50})
c
Tumor
Intratumor
Peri tumor
Far from tumor
300 µm
Bolus
d
Sp3 Pneumonia
Adjacent
Infected
500 µm
Bolus
Structure
Neutrophils
e
Normalized Intensity
Healthy mean
Healthy S.E.
T_{50}
Intratumor mean
Intratumor S.E.
Peritumor mean
Peritumor S.E.
Far from tumor mean
Far from tumor S.E.
Within Sp3 infection mean
Within Sp3 infection S.E.
ΔTime (s)
f
Normalized Max Intensity
p=0.001
p=0.054
p=0.075
p = 0.308
Intratumor
Peritumor
Far from tumor
Within Sp3 infection
Adjacent to Sp3 infection
g
T_{50} (s)
p=0.09
p=0.07
p=0.41
p=0.10
p=0.078
p=0.16
p=0.45
p=0.98
p=0.83
Intratumor
Peritumor
Far from tumor
Healthy
Within Sp3 infection
Adjacent to Sp3 infection
h
Dye (mg/ml)
Step Bolus
Time (min)
i
T = 0 min
T = 60 min
200 µm
Bolus
Intratumor
j
tumor over vessel intensity
Time (min)

Fig. 5. Vascular transport dynamics in health, metastatic cancer, and pneumonia injury. (a) Bolus schematic. **(b)** Representative single tumor image with intratumor, peritumor, and far from tumor regions with corresponding time to peak intensity, normalized maximum pixel intensity, and duration of intensity. **(c)** Time series of pixel intensity in intratumor, peritumor, and far from tumor regions with quantitative time to peak intensity, normalized maximum pixel intensity, and duration of intensity. **(d)** Representative pneumonia injured and adjacent regions with corresponding time to peak intensity, normalized maximum pixel intensity, and duration of intensity. **(e)** Time series of pixel intensity in healthy (n = 5 mice; five R.O.I.s), tumor (n = 4 mice; eight R.O.I.s) and pneumonia (n = 3 mice; five R.O.I.s) conditions with corresponding **(f)** normalized maximum pixel intensity for tumor and pneumonia conditions. **(g)** The. duration of time where the fluorescent intensity is greater than 50% of maximum intensity, T_{50}. is more heterogenous in the intratumor and within pneumonia regions compared to other healthy regions. **(h)** Step bolus schematic. Representative diffusion image at **(i)** t = 0 and t = 60 minutes for single tumor, and **(j)** the tumor to baseline intensity ratio for multiple tumors over time (n = 2 mice; reported as mean ± S.E.M). Box charts indicate median, upper and lower quartiles, and maximum and minimum values that are not outliers of the scattered datapoints.

Discussion:

We have presented the development, validation, and several key applications of the Lung*E*x platform for multiscale imaging of the whole, functional mouse lung in real-time. Whereas previous methods (i) do not resolve micro-scale features (such as in MRI, CT), (ii) provide no temporal resolution, lose the 3D architecture and functional air-liquid interface (such as in histology), or (iii) lack respiratory motion within a small field of view (such as in intravital microscopy[1,3]), the crystal ribcage supports multiscale and high spatiotemporal resolution imaging of the whole organ with near-*in vivo* boundary conditions to capture dynamic functions of the lung simultaneously over almost the entire surface of the lung. We have applied Lung*E*x to image a wide range of lung dynamic (dys)functions at multiple spatial scales including alveolar deformation and elasticity, capillary distensibility, cellular deformation, trafficking and migration of immune cells, and vascular transport. We demonstrated the capabilities of Lung*E*x in health and pathologies such as nodular and infiltrative lung metastases, pneumonia, acute lung injury, and pulmonary fibrosis. Furthermore, this transformative platform offers a wide range of applications to mechanistically probe pathophysiologies relevant to the lung parenchyma such as in emphysema, adenocarcinoma, ventilation-induced lung injury, and dysfunction of blood and lymphatic vessels in aging and lung transplantation.

A unique advantage of Lung*E*x over *in vivo* models is the capability to intervene and precisely control the key respiratory and circulatory parameters. Moreover, combined with the ability to image the lung parenchyma, our approach can establish causal links between physical, biological, and immunological determinants of lung homeostasis and pathophysiology. For example, we have demonstrated that a change in alveolar pressure produces differential strains in healthy vs metastatic, pneumonic, and fibrotic lungs at the sub-alveolar scales (Fig. 2, 3). We utilized the unique ability of Lung*E*x to independently tune parameters to demonstrate how circulation and respiration are coupled and reported an optimum alveolar pressure range in which vascular resistance achieves a minimum at the arteriole/venule level (Fig. 3). Recapitulating the heterogeneities in vascular pressure (e.g., apex vs base [37]), we applied different hydrostatic vascular pressure in models of pneumonia and acute lung injury, and showed that neutrophil migration is highly and reversibly responsive to hydrostatic pressure (Fig. 4). Finally, we probed spatiotemporal vascular transport under controlled alveolar and vascular parameters and quantified the heterogeneities in vascular transport dynamics that vary dramatically in healthy vs nodular lung metastases and pneumonia (Fig. 5). Overall, Lung*E*x uniquely combines the

perturbation/intervention capabilities of lung-on-chip models [9,38] with the multiscale and high spatiotemporal imaging of the whole-lung that preserves the functional complexities and cellular diversity of the lung in health and disease.

We conducted most experiments presented here inside the rigid crystal ribcage for the ease of strain- and age-specific fabrication process. While lacking the flexibility of the PDMS crystal ribcage, which can be utilized to probe the role of ribcage elasticity in breathing mechanics, the rigid crystal ribcage can support negative-pressure ventilation. Therefore, the rigid crystal ribcage can be utilized in comparing the negative- vs. positive-pressure ventilations, and probe the potentially damaging effects of positive-pressure mechanical ventilations [39] at the alveolar and capillary levels. We chose to design a mouse ribcage to take advantage of the wide range of transgenic and reporter mice and the established mouse models of pulmonary diseases to gain a mechanistic understanding of lung pathology. We, however, are aware that mouse models are limited in their ability to recapitulate certain large animal and human (patho)physiologies. Examples include the effect of gravity on lung (dys)function such as in prone vs. supine positioning that affects lung physiology in patients with acute respiratory distress syndrome (ARDS) [40]. Another example is the challenges associated with modeling diseases such as SARS-CoV-2 in mice where the relevant receptors are not expressed. To address these limitations, a large animal or human crystal ribcage would be advantageous. The scalability and ease of fabrication of the rigid crystal ribcage will allow future development of large animal and human-specific crystal ribcages to probe human lung (transplant-rejected cases) at high spatiotemporal resolution and under controlled physiological parameters via the Lung*E*x platform.

In this study, we primarily probed lung functions under quasi-static conditions to decouple effects such as viscoelasticity from equilibrium elasticity, and fluid flow from hydrostatic pressure and thereby reduce the number of confounding factors in our measurements. However, by utilizing ultrafast volumetric imaging techniques, such as light sheet microscopy (e.g., SCAPE [41]), Lung*E*x can be utilized to resolve events at physiologically relevant respiration and circulation time scales to image dynamic coupling between circulation and respiration, cell-cell communications such as calcium signaling, and mapping out viscoelastic and energy dissipation at the alveolar level.

We focused on probing lung (patho)physiology for 4-6 hours postmortem *ex vivo* inside the crystal ribcage, which is a sufficient timescale to study key dynamic events such as mechanical deformation, immune cell migration, and vascular transport dynamics. Disease models such as metastatic cancer and pneumonia were developed in the *in vivo* mouse on the order of days and weeks, while the real-time microscopy components were performed within 4-6 hours *ex vivo*. However, based on previous *ex vivo* studies human lungs have been maintained for up to 24 hours, [42], pig lungs up to 3 days [43] and rat up to 7 days[14]. Utilizing these advances, and the optimized perfusates for prolonged *ex vivo* maintenance of the lung [44], we will adapt Lung*E*x to maintain mouse lung for multi-day imaging. This will open our platform to studying longer-term disease dynamics, as well as motivate new strategies for improving donor lung preservation over time. Specifically, given Lung*E*x enables real-time imaging of lung injury and consequent alveolar flooding at the single alveolus level, our platform can be utilized to answer the longstanding questions surrounding why lungs cannot be maintained *ex vivo* for an extended amount of time[17].

While Lung*E*x allows probing several lung diseases with parenchymal presentation, deeper imaging could broaden the capabilities of our platform. The depth limitation in Lung*E*x is intrinsically associated to optical imaging due to refraction of light at the air-liquid interface [6,9], and not because of the properties of the crystal ribcage. Testing different optical imaging modalities, such as laser confocal microscopy, two-photon microscopy, and optical coherence tomography, we were able to resolve health lung structure up to one to two alveoli (50-100 µm) into the surface of the tissue. Interestingly, in cases where the airspace is replaced with liquid or solid phase, such as tumor, edema, and liquid ventilation, Lung*E*x will enable deeper imaging up to 500µm (fig. S15).

Methods:

Mice. Mice were housed and bred under pathogen–free conditions at the Boston University Animal Science Center. All experiments conformed to ethical principles and guidelines under protocols approved by the Boston University Institutional Animal Care and Use Committee. We used 6- to 12-week-old male and female mice for the experimental procedures. Female FVB mice aged 6-8 weeks (JAX #001800, Jackson Labs, ME) were purchased. A breeding pair of transgenic B6.129(Cg)-Gt(ROSA)26Sortm4(ACTB-tdTomato,-EGFP)Luo/J (JAX #007676, Jackson lab, ME) [45], hereafter referred to as mTmG, was purchased to start a colony and was the primary source of all animals for the experiments. Male neutrophil reporter mice B6.Cg-Tg(S100A8-cre,-EGFP)1Ilw/J (JAX #021614) [46] were purchased from JAX and crossed with in-house homozygous mTmG females to breed MRP8-mTmG mice that were used for neutrophil migration dynamics in the Lung*E*x system.

Metastatic cancer model. E0771-H2B-dendra2 mouse cancer cells or MMTV-H2B-dendra2 (both gifts from Rakesh Jain) were used to model breast cancer metastasis to the lung in mTmG and FVB mice, respectively. Cells were cultured in DMEM (Corning) plus 10% fetal bovine serum (Gibco) plus 1% penicillin/streptomycin (Gibco). Cells were harvested at ~80% confluency, washed twice with phosphate buffered saline (PBS), counted, and resuspended in DMEM prior to tail vein injection into mice at a concentration of 2 million per 300uL complete medium. All cell lines tested negative for mycoplasma (Mycoalert Plus Mycoplasma Detection Kit, Lonza, Allendale, NJ), and authenticated before use by IDEXX laboratories (North Grafton, MA). Mice injected with E0771-H2B-dendra2 were sacrificed on days 5-7 post injection for microscopy of mature nodules. Mice injected with MMTV-H2B-dendra2 were sacrificed on days 10-14 for microscopy of mature nodules. For single cell deformation studies, E0771-H2B-dendra2 cells were plasma membrane labeled with 1,1'-Dioctadecyl-3,3,3',3'-Tetramethylindocarbocyanine, 4-Chlorobenzene Sulfonate Salt (DiD, Invitrogen) before imaging, then washed twice with complete cell culture medium and injected intracardiac into the mouse at a concentration of 6 million per 300uL solution.

LPS acute inflammation model. mTmG mice were treated with 100 ug *Escherichia coli* (*E. coli,* serotype O55:B5, Sigma-Aldrich) lipopolysaccharide LPS diluted to 100 ug/60 uL in PBS via intratracheal injection using an angio-catheter as previously described [47], to model acute injury.

Mice were sacrificed 3-4 hours post induction for microscopy of the acutely injured tissue in the *ex vivo* lung.

Bacterial pneumonia model. We induced bacterial pneumonia in mice as previously described [32]. Briefly, *S. pneumoniae* serotype 3 (Sp3) (ATCC; Manassas, VA) was cultured on plates of BBL Trypticase Soy Agar with 5% sheep blood (BD Trypticase Soy Agar II) (BD Biosciences) in a 37°C humidified 5% CO2 environment for 10-11 hours and diluted in 0.9% sodium chloride to the desired optical density. Mice were anesthetized using a ketamine/xylazine cocktail (100 and 10 mg/kg, respectively) and approximately two million CFU in 50µl were instilled into the left lung lobe via the left bronchus, accessed through the surgically exposed trachea.

Pulmonary fibrosis model. Bleomycin was delivered to the lungs as previously described [26]. Mice were anesthetized with ketamine/xylazine cocktail (100 and 10 mg/kg, respectively) and injected intraperitoneally. About 1 U/Kg bleomycin (APP Pharmaceutical, LCC Schaumburg, IL, USA) was intratracheally delivered using a 30G insulin syringe. Mice were sacrificed for microscopy of fibrotic injuries 113-4 days after injection.

Tissue preparation. Isolated mouse lungs were ventilated through a tracheal cannula and perfused through two cannulas inserted into the pulmonary artery (PA) and left atrium as previously described [48]. Perfusions included whole blood, cellular, or acellular media containing fluorescent labels for vascular lumens and circulating cells. After cannulation, the lung-heart bloc was placed into the crystal ribcage for microscopy under controlled ventilation/circulation parameters. The lung was ventilated *ex vivo* using a (Kent Physiosuite Mouse ventilator, Kent Scientific) or held at static alveolar pressure using an air-filled vinyl tube submerged in a water column. Perfusion pressure was controlled using a 60 ml reservoir containing the perfusate medium (serum-free RPMI, Gibco) suspended at different hydrostatic heights above the height of the lung.

In situ imaging ribcage preparation. Mice were anesthetized as described above and ventilated through a tracheal cannula. The mouse was sacrificed at this point ensuring the lungs did not collapse but maintain a positive end expiratory pressure (PEEP) of 5-7 cmH_2O. The skin and fascia were dissected away and then the intercostal muscles between the ribs was carefully separated under a stereomicroscope till the underlying ribcage pleura was visible. A 2mm x 3mm retaining clamp was inserted in the cleared section to prevent the leftover tissue strands blocking the opening. The PEEP on the lung was altered to confirm that the lung-maintained contact with the internal pleural membrane and that the lung was responsive to pressure changes. The mouse chest carcass was angled upwards for imaging.

Ex vivo lung microscopy. Prepared *ex vivo* lungs inside the crystal ribcage were imaged using an inverted laser-scanning confocal microscope (Olympus FV 3000) under objective magnifications of 1.25x, 10x, and 20x, with environmental temperature control set to 37℃. Additionally, lungs were imaged using an upright Nikon fluorescent stereomicroscope, a ThorLabs upright optical coherence tomography probe and an upright Bruker two-photon microscope.

Mouse ribcage 3D object creation. Previously recorded pressure controlled µCT scans of C57B/6 and AJ mice chest cavities were obtained from the Hoffman group at the University of Iowa [15-17]. These scans were segmented in MATLAB (v. R2019b Mathworks, Natick MA) using a custom

algorithm and user defined regions of interest to obtain a coarse 3D object that represented the mouse chest cavity including a small section of the trachea. This coarse 3D binary object was refined and re-meshed in Meshmixer (Autodesk) to remove any sharp edges and make a stereolithography (STL) object. The Meshmixer files were imported into Solidworks 2019 (Dassault systems, France) to add registration features prior to 3D printing. The model was made age-specific by scaling the binary object by mouse lung volume reported by age [49] (fig. S1). The final STL file was printed using FormLabs (Somerville, MA) clear resin on a Form3 printer and additionally post-cured for 30 minutes. The final 3D printed insert was washed and polished to remove any layer lines and obtain a high gloss finish on the surface.

PDMS ribcage fabrication. The 3D printed lung insert was used to make a negative mold by embedding it in a soft silicone-based elastomer called Ecoflex 00-30 (Smooth-On Inc, Macungie PA) under vacuum for 5 hours. Post curing the 3D insert was removed to obtain a smooth exact negative mold. The internal surface of the mold was coated with a thin layer of PDMS to completely seal it from air and make the internal geometry rigid. The negative space was slowly filled with a casting sugar solution that was kept liquid at ~140˚C. The sugar filled mold was degassed in the oven for over an hour to remove any trapped air bubbles in the sugar, cured by cooling over 2 hours at room temperature, and then gently removed by deforming the soft silicone mold. Polymethyldisiloxane (PDMS) was mixed in a standard 10:1 monomer to crosslinker ratio and gradually poured over the sugar mold, completely covering the surface, and then set to partially cure at ~50˚C for 25-30 minutes. This was repeated five times after which it was left to cure for 12-18 hours at ~50˚C in a dehydrating oven. The cast PDMS was positioned in a 3D printed crystal ribcage support and attached with dabs of glue. The assembly was then left in lukewarm water for 2-3 hours to dissolve the cast sugar to obtain the PDMS crystal ribcage.

Polystyrene ribcage fabrication. The 3D printed insert was positioned over a miniature dental thermoforming device. A 0.7mm clear polystyrene sheet was fed into the device and allowed to heat before it was pulled over the 3D printed insert while applying a vacuum to remove any trapped air between the mold and the polystyrene. The heat and vacuum were turned off and the formed polystyrene was removed from over the mold using compressed air. This rigid crystal ribcage was fitted into a support neck and fused by friction welding and using cyanoacrylate glue.

Crystal ribcage surface treatment. Both rigid and deformable crystal ribcage surfaces have native hydrophobic surfaces which were engineered to be hydrophilic by treating with oxygen plasma using a Harrick Plasma Cleaner. The crystal ribcages were subjected to a vacuum of 800-900mTorr and then subjected to plasma treatment at medium power for 2 minutes.

Ventilation pressure and flow sensor calibration. Ventilation pressure sensors SSDRRV100MDAA5 (Honeywell Inc.) were rated to measure between ±100 cmH_2O with a 0-5V linearly scaled output. The pressure sensor was calibrated prior to every experiment with a simple water column between 0-10 cmH_2O and the calibration value was used to scale the raw voltage into pressure values in real-time. The flow sensor was calibrated one-time when it was assembled using a 3D printed constriction and SSDRRV010MDAA5 (Honeywell Inc.) differential ±10 cmH_2O linearly scaled pressure sensor. The obtained voltage-flow curve which was fitted to a reflected power curve to obtain the flow values in ml/min for a given change in resistance read

across the sensor. All sensor readings were scaled to real units using an Arduino and custom MATLAB functions to display in real-time.

Perfusion pressure and flow sensor calibration. Perfusion was measured with 26PCAFG6G (Honeywell Inc.) that were rated between 0 to 1 PSI unamplified gauge pressure sensors. The pressure sensor was read into an HX711 analog to digital converter before being read on an onboard Arduino Uno. The scaled digital values were calibrated against a known water column between 0-10 cmH_2O prior to every experiment. The perfusion flow was measured using a small form factor Sensirion SLF-1300F liquid flow sensor. The sensor comes factory calibrated for DI water and 70% ethanol. It was calibrated for different perfusates by linearly scaling the sensor reading with a known syringe pump driven flow prior to the experiment. All sensor readings were scaled to real units using an Arduino and custom MATLAB functions to display them in real-time.

Versatile microscopy arm. We developed two custom microscopy arms using commercially available photography brackets to allow both 3- and 6-degrees of freedom to orient the crystal ribcage with available upright (fluorescent stereomicroscope, multi-photon microscope, optical coherence tomography) or inverted microscopes (laser scanning confocal microscope) (fig. S4). We successfully tested our mounting arm to image the lung surface with the above microscopes and with a wide range of objective power, ranging from 1.25x (lobe-scale), 10x (alveolar-scale), and 40x (subcellular-scale) imaging of the same lung.

Alveolar diameter measurement. Microscopy images recorded with a 10x objective and an additional 1.5x optical zoom were loaded into FIJI-ImageJ and sum-wise projected in the z-direction for all pressure conditions. Alveoli common to all pressures were annotated prior to making measurements. The mean alveolar diameter was calculated by recording 2 length values between anatomical features that were diametrically opposite to each other. The mean lengths were recorded for all corresponding alveoli at different pressures. These measurements were compiled in MATLAB to make raincloud plots [50] and compute group-wise statistics.

Single cell measurement. Microscopy images recorded with a 10x objective with a 4x zoom or 20x objective with 4x zoom were loaded into FIJI-ImageJ for all pressure conditions. The maximum plane of the cell was identified by a user and then a freehand trace of the shape of the cell was traced around the cell. Shape parameters including the maximum and minimum Feret diameters were reported by FIJI for every annotation and compiled in MATLAB to perform statistical comparisons between the Feret ratio.

Alveolar septum strain calculation. We used a previously published deformable registration algorithm, deedsBCV [51] to autonomously determine the displacement map between images of the lung tissue at alveolar pressures of 7 and 12 cmH_2O, and subsequently use a custom algorithm to compute the strain map (fig. S16). A cubic smoothing spline was used to approximate the displacement map and evaluate its gradient derivative to then directly calculate the canonical strain tensors (fig. S17). This method gives us a displacement gradient continuous in its second derivatives which prevents obscuring the true signal in the noise. We validated the effect of the smoothing spline on the original and target images to ensure accurate registration between them by using multiple kernel sizes to ensure that the final registered image matches the target image. The strain computation was then validated for known synthetic displacement maps (fig. S18) to

ensure no fundamental errors existed between the mathematical ground truth and image-based strain estimation.

Cell tracking for neutrophil migration. Post-processing of neutrophil migration data was performed in MATLAB. Multi-channel recordings from microscopy were stabilized and single neutrophil centroids were computed per frame to obtain corresponding position and speed information. Persistence was calculated as the total displacement divided by contour length of the path. Where relevant, migration through the intravascular space was defined as movement confined within the vasculature, intra-alveolar as movement within alveolar spaces, and interstitial as those crossing between vascular and alveolar spaces. Neutrophil shape was segmented using an intensity threshold and the *regionprops* function was used to compute aspect ratio and circularity.

Perfusion and vascular transport. Mouse lungs were perfused with serum-free RPMI at 37°C. To model small molecule drug transport, 50 μL of Cascade Blue dextran (10 kDa, Molecular Probes) or Cascade Blue hydrazide trisodium salt (500 Da, Invitrogen) were injected into the perfusion tubing upstream of the pulmonary artery cannula at a concentration of 10 mg/ml over approximately 1 second. Vascular dynamics were imaged over time using a laser-scanning confocal microscope (Olympus FV3000). Post-processing of vascular transport data was performed in MATLAB. Microscopy recording channels corresponding to impulse bolus injection were down sampled to a mesh grid with single pixel dimensions on the scale of a single alveolus (approximately 50μm). Intratumor regions were segmented based on the presence of fluorescently labeled tumor cells. Within the extratumor regions, the peri-tumor region was thresholded from regions far from the tumor based on a reduction of bolus intensity threshold. Sp3 infected areas were segmented based on the presence of fluorescently labeled neutrophils. Time series of dye intensity was normalized to the maximum mean intensity of each video (normalized maximum intensity). The duration of dye intensity greater than 50% of the normalized maximum intensity was calculated (T_{50}). The time from initial increase in pixel intensity time series to the normalized maximum intensity was calculated (T_{max}). Step bolus injections for tumor diffusion were processed in ImageJ to obtain dye intensity intratumor and baseline intensity measured within the vasculature.

Statistical analyses. The data are presented as mean ± standard error of the mean. All statistics calculated as Student's t-test to determine significance or p-values between groups of data. All p-values < 0.1 are reported on figures for the users to observe statistical trends of data.

Acknowledgements: We thank the Neurophotonics Center at Boston University for their generous support and access to their facility. Adam Coats from the Hoffman lab at the University of Iowa provided the μCT image data sets used to fabricate the crystal ribcage. The research reported in this publication was supported by the Boston University Micro and Nano Imaging Facility and the Office of the Director, National Institutes of Health of the National Institutes of Health under award Number S10OD024993. The content is solely the responsibility of the authors and does not necessarily represent the official views of the National Institute of Health.

Funding: H.T.N. discloses support for the research described in this study from the National Institutes of Health R21EB031332 and DP2HL168562, Beckman Young Investigator Award, Boston University Center for Multiscale and Translational Mechanobiology, and Dean's Catalyst Award, and the American Cancer Society Institutional Fund at Boston University.

Author contributions: R.B., G.N.G. and H.T.N. conceived the project and wrote the manuscript; R.B. developed and validated the Lung*E*x platform and the crystal ribcage, established transgenic mouse colonies, analyzed alveolar mechanics data, G.N.G. conducted the lung extraction and imaging, generated experimental mice, developed vascular distensibility calculation workflow; L.S. developed neutrophil tracking, deformation and migration analysis codes, and analyzed vascular transport data; D.S. calculated alveolar diameters and single cell morphology, and maintained animal colony; R.L. adapted deformable image registration and developed strain analysis code for application in microscopy images; J.M. maintained the Lung*E*x system and calculated alveolar diameters; C.E. developed fabrication process of deformable crystal ribcage; B.H. cultured and instilled *S. pneumoniae* to generate lobar pneumonia model; J.L. treated mice with bleomycin to generate fibrosis model; K.R. and S. Z. assisted with culture of cancer cells; S.S.Z. fabricated fluorescent polyacrylamide beads; J.J. assisted in developing surgical technique for *in vivo* imaging of lung tissue; R.P. trained G.G. on LPS model induction and performed proof of concept experiments; K.T. provided transgenic MPR8-Cre$^+$ mouse to help establish neutrophil-reporter mouse colony; G.L., J.P.M. and B.S. contributed to discussion on crucial aspects of the project; H.T.N. supervised the project and provided guidance on experimental design, data collection, data interpretation and writing of the manuscript.

Competing interests: Authors declare that they have no competing interests.

Data and materials availability: All data are available in the main text or the supplementary materials. Raw data and code for analysis are available upon request.

References:

1 Looney, M. R. *et al.* Stabilized imaging of immune surveillance in the mouse lung. *Nat Methods* **8**, 91-96 (2011). https://doi.org:10.1038/nmeth.1543

2 Headley, M. B. *et al.* Visualization of immediate immune responses to pioneer metastatic cells in the lung. *Nature* **531**, 513-517 (2016). https://doi.org:10.1038/nature16985

3 Entenberg, D. *et al.* A permanent window for the murine lung enables high-resolution imaging of cancer metastasis. *Nat Methods* **15**, 73-80 (2018). https://doi.org:10.1038/nmeth.4511

4 Ueki, H., Wang, I. H., Zhao, D., Gunzer, M. & Kawaoka, Y. Multicolor two-photon imaging of in vivo cellular pathophysiology upon influenza virus infection using the two-photon IMPRESS. *Nat Protoc* **15**, 1041-1065 (2020). https://doi.org:10.1038/s41596-019-0275-y

5 Westphalen, K. *et al.* Sessile alveolar macrophages communicate with alveolar epithelium to modulate immunity. *Nature* **506**, 503-506 (2014). https://doi.org:10.1038/nature12902

6 Lefrancais, E. *et al.* The lung is a site of platelet biogenesis and a reservoir for haematopoietic progenitors. *Nature* **544**, 105-109 (2017). https://doi.org:10.1038/nature21706

7 Borriello, L. *et al.* Primary tumor associated macrophages activate programs of invasion and dormancy in disseminating tumor cells. *Nat Commun* **13**, 626 (2022). https://doi.org:10.1038/s41467-022-28076-3

8 Kreisel, D. *et al.* In vivo two-photon imaging reveals monocyte-dependent neutrophil extravasation during pulmonary inflammation. *Proc Natl Acad Sci U S A* **107**, 18073-18078 (2010). https://doi.org:10.1073/pnas.1008737107

9 Hassell, B. A. *et al.* Human Organ Chip Models Recapitulate Orthotopic Lung Cancer Growth, Therapeutic Responses, and Tumor Dormancy In Vitro. *Cell Rep* **21**, 508-516 (2017). https://doi.org:10.1016/j.celrep.2017.09.043

10 Haudebourg, A. F. *et al.* Respiratory Mechanics of COVID-19- versus Non-COVID-19-associated Acute Respiratory Distress Syndrome. *Am J Respir Crit Care Med* **202**, 287-290 (2020). https://doi.org:10.1164/rccm.202004-1226LE

11 Lederer, D. J. & Martinez, F. J. Idiopathic Pulmonary Fibrosis. *N Engl J Med* **378**, 1811-1823 (2018). https://doi.org:10.1056/NEJMra1705751

12 Suki, B. *et al.* Emphysema and mechanical stress-induced lung remodeling. *Physiology (Bethesda)* **28**, 404-413 (2013). https://doi.org:10.1152/physiol.00041.2013

13 Hozain, A. E. *et al.* Xenogeneic cross-circulation for extracorporeal recovery of injured human lungs. *Nat Med* **26**, 1102-1113 (2020). https://doi.org:10.1038/s41591-020-0971-8

14 Petersen, T. H., Calle, E. A., Colehour, M. B. & Niklason, L. E. Bioreactor for the long-term culture of lung tissue. *Cell Transplant* **20**, 1117-1126 (2011). https://doi.org:10.3727/096368910X544933

15 Kizhakke Puliyakote, A. S. *et al.* Morphometric differences between central vs. surface acini in A/J mice using high-resolution micro-computed tomography. *J Appl Physiol (1985)* **121**, 115-122 (2016). https://doi.org:10.1152/japplphysiol.00317.2016

16 Vasilescu, D. M. *et al.* Stereological assessment of mouse lung parenchyma via nondestructive, multiscale micro-CT imaging validated by light microscopic histology. *J*

Appl Physiol (1985) **114**, 716-724 (2013). https://doi.org:10.1152/japplphysiol.00855.2012
17 Thiesse, J. *et al.* Lung structure phenotype variation in inbred mouse strains revealed through in vivo micro-CT imaging. *J Appl Physiol (1985)* **109**, 1960-1968 (2010). https://doi.org:10.1152/japplphysiol.01322.2009
18 Hall, J. E. *Guyton and hall textbook of medical physiology*. 14. edn, (Elsevier, 2020).
19 Haak, A. J. *et al.* Selective YAP/TAZ inhibition in fibroblasts via dopamine receptor D1 agonism reverses fibrosis. *Sci Transl Med* **11** (2019). https://doi.org:10.1126/scitranslmed.aau6296
20 Stella, G. M., Kolling, S., Benvenuti, S. & Bortolotto, C. Lung-Seeking Metastases. *Cancers (Basel)* **11** (2019). https://doi.org:10.3390/cancers11071010
21 Nia, H. T. *et al.* Solid stress and elastic energy as measures of tumour mechanopathology. *Nat Biomed Eng* **1** (2016). https://doi.org:10.1038/s41551-016-0004
22 Nia, H. T., Munn, L. L. & Jain, R. K. Physical traits of cancer. *Science* **370** (2020). https://doi.org:10.1126/science.aaz0868
23 Seano, G. *et al.* Solid stress in brain tumours causes neuronal loss and neurological dysfunction and can be reversed by lithium. *Nat Biomed Eng* **3**, 230-245 (2019). https://doi.org:10.1038/s41551-018-0334-7
24 Eefsen, R. L. *et al.* Growth pattern of colorectal liver metastasis as a marker of recurrence risk. *Clin Exp Metastasis* **32**, 369-381 (2015). https://doi.org:10.1007/s10585-015-9715-4
25 Wang, G. *et al.* Identification of the Transgene Integration Site and Host Genome Changes in MRP8-Cre/ires-EGFP Transgenic Mice by Targeted Locus Amplification. *Front Immunol* **13**, 875991 (2022). https://doi.org:10.3389/fimmu.2022.875991
26 Caporarello, N. *et al.* Dysfunctional ERG signaling drives pulmonary vascular aging and persistent fibrosis. *Nat Commun* **13**, 4170 (2022). https://doi.org:10.1038/s41467-022-31890-4
27 West, J. B. & Luks, A. M.
28 Quinton, L. J., Walkey, A. J. & Mizgerd, J. P. Integrative Physiology of Pneumonia. *Physiol Rev* **98**, 1417-1464 (2018). https://doi.org:10.1152/physrev.00032.2017
29 Lefrancais, E., Mallavia, B., Zhuo, H., Calfee, C. S. & Looney, M. R. Maladaptive role of neutrophil extracellular traps in pathogen-induced lung injury. *JCI Insight* **3** (2018). https://doi.org:10.1172/jci.insight.98178
30 Domscheit, H., Hegeman, M. A., Carvalho, N. & Spieth, P. M. Molecular Dynamics of Lipopolysaccharide-Induced Lung Injury in Rodents. *Front Physiol* **11**, 36 (2020). https://doi.org:10.3389/fphys.2020.00036
31 Mitchell, M. J., Lin, K. S. & King, M. R. Fluid shear stress increases neutrophil activation via platelet-activating factor. *Biophys J* **106**, 2243-2253 (2014). https://doi.org:10.1016/j.bpj.2014.04.001
32 Barker, K. A. *et al.* Lung-resident memory B cells protect against bacterial pneumonia. *J Clin Invest* **131** (2021). https://doi.org:10.1172/JCI141810
33 Fine, N., Dimitriou, I. D. & Rottapel, R. Go with the flow: GEF-H1 mediated shear stress mechanotransduction in neutrophils. *Small GTPases* **11**, 23-31 (2020). https://doi.org:10.1080/21541248.2017.1332505
34 Niethammer, P. Neutrophil mechanotransduction: A GEF to sense fluid shear stress. *J Cell Biol* **215**, 13-14 (2016). https://doi.org:10.1083/jcb.201609101

35 Finger, E. B. *et al.* Adhesion through L-selectin requires a threshold hydrodynamic shear. *Nature* **379**, 266-269 (1996). https://doi.org:10.1038/379266a0
36 Thibault, H. B. *et al.* Noninvasive assessment of murine pulmonary arterial pressure: validation and application to models of pulmonary hypertension. *Circ Cardiovasc Imaging* **3**, 157-163 (2010). https://doi.org:10.1161/CIRCIMAGING.109.887109
37 Galvin, I., Drummond, G. B. & Nirmalan, M. Distribution of blood flow and ventilation in the lung: gravity is not the only factor. *Br J Anaesth* **98**, 420-428 (2007). https://doi.org:10.1093/bja/aem036
38 Huh, D. *et al.* Reconstituting organ-level lung functions on a chip. *Science* **328**, 1662-1668 (2010). https://doi.org:10.1126/science.1188302
39 Sattari, S. *et al.* Positive- and Negative-Pressure Ventilation Characterized by Local and Global Pulmonary Mechanics. *Am J Respir Crit Care Med* (2022). https://doi.org:10.1164/rccm.202111-2480OC
40 Guerin, C. *et al.* Prone positioning in severe acute respiratory distress syndrome. *N Engl J Med* **368**, 2159-2168 (2013). https://doi.org:10.1056/NEJMoa1214103
41 Voleti, V. *et al.* Real-time volumetric microscopy of in vivo dynamics and large-scale samples with SCAPE 2.0. *Nat Methods* **16**, 1054-1062 (2019). https://doi.org:10.1038/s41592-019-0579-4
42 Cardenes, N. *et al.* Human ex vivo lung perfusion: a novel model to study human lung diseases. *Sci Rep* **11**, 490 (2021). https://doi.org:10.1038/s41598-020-79434-4
43 Ali, A. *et al.* Successful 3-day lung preservation using a cyclic normothermic ex vivo lung perfusion strategy. *EBioMedicine* **83**, 104210 (2022). https://doi.org:10.1016/j.ebiom.2022.104210
44 Loor, G. *et al.* Prolonged EVLP Using OCS Lung: Cellular and Acellular Perfusates. *Transplantation* **101**, 2303-2311 (2017). https://doi.org:10.1097/TP.0000000000001616
45 Muzumdar, M. D., Tasic, B., Miyamichi, K., Li, L. & Luo, L. A global double-fluorescent Cre reporter mouse. *Genesis* **45**, 593-605 (2007). https://doi.org:10.1002/dvg.20335
46 Passegue, E., Wagner, E. F. & Weissman, I. L. JunB deficiency leads to a myeloproliferative disorder arising from hematopoietic stem cells. *Cell* **119**, 431-443 (2004). https://doi.org:10.1016/j.cell.2004.10.010
47 Mizgerd, J. P., Scott, M. L., Spieker, M. R. & Doerschuk, C. M. Functions of IkappaB proteins in inflammatory responses to Escherichia coli LPS in mouse lungs. *Am J Respir Cell Mol Biol* **27**, 575-582 (2002). https://doi.org:10.1165/rcmb.2002-0015OC
48 Vanderpool, R. R. & Chesler, N. C. Characterization of the isolated, ventilated, and instrumented mouse lung perfused with pulsatile flow. *J Vis Exp* (2011). https://doi.org:10.3791/2690
49 Schulte, H., Muhlfeld, C. & Brandenberger, C. Age-Related Structural and Functional Changes in the Mouse Lung. *Front Physiol* **10**, 1466 (2019). https://doi.org:10.3389/fphys.2019.01466
50 Allen, M., Poggiali, D., Whitaker, K., Marshall, T. R. & Kievit, R. A. Raincloud plots: a multi-platform tool for robust data visualization. *Wellcome Open Res* **4**, 63 (2019). https://doi.org:10.12688/wellcomeopenres.15191.1
51 Heinrich, M. P., Jenkinson, M., Brady, M. & Schnabel, J. A. MRF-based deformable registration and ventilation estimation of lung CT. *IEEE Trans Med Imaging* **32**, 1239-1248 (2013). https://doi.org:10.1109/TMI.2013.2246577